11-2018

A Statistical Analysis of STEVE

Bea Gallardo-Lacourt

Y. Nishimura

E. Donovan

G. W. Gillies

W. E. Archer

See next page for additional authors

Recommended Citation

Gallardo-Lacourt, B., et al. (2018). A Statistical Analysis of STEVE. Journal of Geophysical Research: Space Physics, 123(11), 9893–9905. https://doi.org/10.1029/2018JA025368

Gallardo-Lacourt Bea (Orcid ID: 0000-0003-3690-7547)
Nishimura Toshi (Orcid ID: 0000-0003-3126-4394)
Gillies D. Megan (Orcid ID: 0000-0001-9608-797X)
Perry Gareth, William (Orcid ID: 0000-0002-4690-5783)
Archer William, Edward (Orcid ID: 0000-0003-2292-6173)
Spanswick Emma (Orcid ID: 0000-0001-8003-5091)

A Statistical Analysis of STEVE

Bea Gallardo-Lacourt [1], Y. Nishimura [2,3], E. Donovan[1], D. M. Gillies[1], G. W. Perry[1], W.E. Archer[4], O. A. Nava[5], and E. L. Spanswick[1]

1 Department of Physics and Astronomy, University of Calgary, Calgary, Alberta, Canada.

2 Department of Electrical and Computer Engineering and Center for Space Physics, Boston University, Boston, Massachusetts, USA

3 Department of Atmospheric and Oceanic Sciences, University of California, Los Angeles, California, USA

4 Department of Physics and Engineering Physics, University of Saskatchewan, Saskatoon, Saskatchewan, Canada

5 Department of Engineering Physics, Air Force Institute of Technology, Wright-Patterson Air Force Base, Ohio, USA

Bea Gallardo-Lacourt, E. Donovan, G. W. Perry, D. M. Gillies, and E. L. Spanswick at Department of Physics and Astronomy, University of Calgary, Calgary, AB T2N 1N4, Canada. (beatriz.gallardo@ucalgary.ca)

Y. Nishimura at Department of Atmospheric and Oceanic Sciences, University of California, Los Angeles, 405 Hilgard Ave., Los Angeles, CA 90095-1565, USA.

W. E. Archer at Department of Physics and Engineering Physics, University of Saskatchewan, 116 Science Pl, Saskatoon, SK S7N 5E2, Canada.

This is the author manuscript accepted for publication and has undergone full peer review but has not been through the copyediting, typesetting, pagination and proofreading process, which may lead to differences between this version and the Version of Record. Please cite this article as doi: 10.1029/2018JA025368

Key Points

- First statistical study of the subauroral optical phenomenon known as STEVE, featuring 28 events identified with all-sky imagers.
- STEVE is a latitudinally narrow optical structure: ~20 km in meridional spread and spanning over 2000 km zonally.
- STEVE is strongly linked to substorms: it is observed subsequent to a prolonged (~1 hour) substorm expansion phase.

Abstract

There has been an exciting recent development in auroral research associated with the discovery of a new subauroral phenomenon called STEVE (Strong Thermal Emission Velocity Enhancement). Although STEVE has been documented by amateur night sky watchers for decades, it is as yet an unidentified upper atmosphere phenomenon. Observed first by amateur auroral photographers, STEVE appears as a narrow luminous structure across the night sky over thousands of kilometers in the east-west direction. In this paper, we present the first statistical analysis of the properties of 28 STEVE events identified using THEMIS ASI and the REGO database. We find that STEVE occurs about one hour after substorm onset at the end of a prolonged expansion phase. On average, the AL index magnitude is larger and the expansion phase has a longer duration for STEVE events compared to SAIDs or substorms. The average duration for STEVE is about one hour and its latitudinal width is ~20km, which corresponds to ~ ¼ of the width of narrow auroral structures like streamers. STEVE typically has an equatorward displacement from its initial location of about 50 km and a longitudinal extent of 2145 km.

Plain Language Summary

STEVE is an atmospheric phenomenon that manifests across the night-sky as an extremely thin yet long ribbon of vibrant purple and white hues. Although STEVE has been well-documented by amateur auroral photographers for several decades, the scientific community only recently stumbled upon this phenomenon. In this paper, we report on the first statistical analysis of STEVE's optical characteristics using ground-based all-sky imagery and examined satellite data to determine the geomagnetic conditions favorable for the formation of STEVE. Our results verify that STEVE is narrow in the north-south direction, but it extends over a wider east-west region. We have also determined that STEVE displaces southward over its lifetime in most observations. More interestingly, all 28 STEVE events identified in this study were observed at the end of a prolonged substorm expansion phase.

1. Introduction

Recently, the scientific community stumbled upon a phenomenon that was well known to amateur auroral enthusiasts and has been called 'Steve'. Observed in the images of amateur photographers, this new phenomenon is a mauve and green narrow band of light that appears distinctly different from traditional auroral structures. MacDonald et al. [2018] reported a 'Steve' event observed by ground optical data in conjunction with Swarm satellite measurements. In the optical data from the Redline Geospace Observatory (REGO) All-Sky Camera (ASI) at Lucky Lake (LUCK), 'Steve' develops adjacent to and equatorward of the pre-midnight auroral oval (in the suburoral region) and is observed for approximately one hour across the LUCK Field-of-view (FOV). Its structure extends for thousands of kilometers in the east-west direction but only has a width of tens of kilometers in the north-south direction. During the event reported by MacDonald et al. (2018) the Swarm-A satellite crossed the location of the emission (in REGO's field-of-view) revealing that the observed luminosity was collocated with a very hot stream (~6000° K) of electrons moving very fast (>6 km/sec) in a band with a north-south extent of less than 50 km. Due to these observed characteristics, the name 'Steve' was recast as *Strong Thermal Emission Velocity Enhancement* or STEVE.

More recently, Gallardo-Lacourt et al. [2018] analyzed data from the Polar Orbiting Environmental Satellite (POES)-17 satellite for one STEVE event identified by Time History of Events and Macroscale Interactions during Substorm (THEMIS) ASI. Their results showed an absence of particle precipitation (ions and electrons) at the time the satellite crossed the structure, suggesting that optical emissions of STEVE might not be a result of the aurora, and that its emissions entirely generated within the ionosphere by another mechanism These two studies are the first scientific publications on STEVE, but its properties and occurrence characteristics are still poorly understood.

Stable Auroral Red (SAR) arcs are optical signatures observed in the same region as STEVE, however the two phenomena have several distinct characteristics. The lifetimes of SAR arcs vary from several hours to days [Nagai, 1970] and are characterized by their 'spectral purity' [Kozyra et al., 1997]. In contrast, STEVE persists for approximately one hour and its emission manifests as a mix of purple and white hues a reported by MacDonald et al. [2018] and other events documented by citizen scientists. While the latitudinal extent of SAR arcs can extent several hundred kilometers, STEVE is more narrow --

approximately half a degree in latitude (tens of kilometers). Lastly, SAR arcs are exemplified by their stability – hence the name – whereas STEVE exhibits clear optical signatures of instability and, as we will discuss, latitudinal movement. In this paper we analyze some of the characteristics that make STEVE different from SAR arcs.

In this study, we performed a statistical analysis based on 28 STEVE events identified using THEMIS ASI and the REGO database. In the first part of this study, we characterized STEVE from its optical signature calculating its width, latitudinal displacement, duration, and longitudinal coverage. In the second part, we analyzed solar wind conditions and geomagnetic indices before, during, and after STEVE was observed in the optical data.

We show that STEVE typically occurs about one hour after substorm onset and it is an extremely narrow structure of only ~20 km in latitude. Its longitudinal extent is at least ~2145 km with an average duration of ~1 hour.

2. Dataset and methodology

We characterized 28 STEVE events using the THEMIS ASI dataset and the REGO database. We identified 21 events in THEMIS ASI observations from December 2007 to December 2015 and 7 events in the REGO ASI observations from November 2014 to December 2017.

The THEMIS ASIs are white light CCD imagers, where each imager has a latitudinal coverage of ~9° and a longitudinal coverage of ~2.5h MLT with a time resolution of 3s. The spatial resolution is ~100 m near zenith [Mende et al., 2008] and ~1 km away from zenith in regions where we observed STEVE. There are 21 THEMIS ASIs covering a large section of the North-American auroral oval, providing 2-D observations with high temporal and spatial resolution.

The REGO imagers are designed to measure red-line optical emissions with high sensitivity and temporal resolution. The red-line optical emission is produced by the transition of atomic oxygen from an excited state to the ground state [Solomon et al. 1988; Link and Cogger, 1988, Gillies et al., 2017]. REGO operates at a 3 s cadence with a 2 s exposure time [Liang et al., 2016]. The REGO array is comprised of 9 All-Sky cameras that cover a large portion of the North-American sector. REGO is sensitive to wavelengths between ~628-632 nm, with a maximum at 630 nm [Liang et al., 2016]. As a manifestation

of its sensitivity, the REGO imagers located at poleward latitudes can easily detect faint polar-cap patches—which are often no more than several tens of Rayleigh in intensity—and their subtle spatial/temporal variations [e.g., Zou et al., 2015].

In this study we identified STEVE using the two optical databases described above. Keograms from the camera's central meridian were created to identify STEVE closer to the center of the ASI FOV. A keogram is a north-south slice across the imager (in this case at the central longitude of the ASI) plotted as a function of time.

In the following section of this paper we analyzed STEVE using optical data. Section 3a shows two representative events of STEVE identified in THEMIS ASI and REGO database respectively. In section 3b we calculate STEVE's monthly and yearly occurrence, duration, latitudinal width, latitudinal displacement and longitudinal extent from the 28 events identified in optical data. All of our events were observed between 22-01 MLT.

We also analyzed solar wind conditions for these STEVE events, using the 1 minute resolution OMNI database. From this dataset, we analyzed solar wind dynamic pressure, flow speed, all three components of the Interplanetary Magnetic Field (IMF), AL index and Kp index. In addition, we analyzed Dst indices from the Kyoto database. The findings using this data are presented in Section 4. In this section we also compare STEVE's AL index with those observed for typical substorms. We have used the SuperMAG onset list from 2001 to 2010 comprising more than 16000 substorm events. SuperMAG (http://supermag.jhuapl.edu) is a worldwide collaboration of organizations and national agencies which currently operate more than 300 ground-based magnetometers spread across the globe [Gjerloev, 2009; Gjerloev, 2012]. This substorm list has been derived using an automated algorithm to identify substorm expansion phase onsets using the SML index (SuperMAG equivalent for AL index). The substorm selection criteria requires a sharp and sustained drop [Newell and Gjerloev, 2011].

In addition, we have compared the AL index observed during STEVE with SAID events identified by Archer and Knudsen [2018] in Swarm satellite measurements. Swarm is a constellation of three satellites designed to study the dynamics of the Earth's magnetic field and its interactions with the Earth's system [Olsen et al., 2013]. It was launched in November 2013 in a nearly circular polar noon-to-midnight orbits around 500 km altitude.

3. Characterizing Steve using optical data

3a. Representative events: STEVE observed using THEMIS ASI and REGO data bases

In this section, we present two examples of STEVE events identified using the THEMIS ASI and REGO databases. These events were identified by their distinct morphology. In the optical data, STEVE is observed as a narrow, but wide structure in latitude and longitude, respectively. It is, clearly detached from the auroral oval and located equatorward of it. Figure 1a shows the temporal evolution of STEVE observed at Athabasca (ATHA) ASI. Magnetic midnight for this ASI occurs at ~8:30UT. The white dashed contour corresponds to 60˚ MLat. Initially the auroral oval is located at higher latitudes than the ASI location (panel i). At 05:06:00UT (Panel ii) we start observing the equatorward motion of the auroral oval. At 05:38:00UT (panel iii), STEVE is detected as a faint structure closer to the central latitude of the camera FOV. At 06:07:00UT STEVE is observed as a very narrow and bright structure distinctly located equatorward of the auroral oval. STEVE then becomes fainter and lasts until ~06:20:00UT (panel v).

The keogram (north-south slice in the central meridian of the ATHA ASI) presented in Figure 1b summarizes this event. First STEVE is observed as a faint structure shortly after ~5:30:00UT. Afterwards, the structure moves equatorward and becomes brighter before 06:00:00UT. In this event STEVE is observed as a narrow structure of ~0.5˚ MLat. Located at ~62˚ MLat. This example illustrates clearly that STEVE is located at least 1˚ MLat equatorward than the auroral oval (optical equatorward boundary between 63-64˚ MLat).

Figure 2 shows an example of STEVE observed at LUCK REGO imager on September 27, 2017. Figure 2a shows the 2D evolution of STEVE using Gillam (GILL) and LUCK REGO ASI. Magnetic midnight at the LUCK ASI occurs at ~08:00UT. The white dashed lines represent 55˚ and 65˚ MLat. Unfortunately for this event it was cloudy above GILL, but the evolution of a substorm is observable through clouds. Initially the auroral oval is relatively quiet (panel i). At 06:08:00UT (panel ii) the beginning of the expansion phase can be observed by the enhanced luminosity observed in GILL. At around 06:50UT STEVE is first detected as a very faint structure equatorward of the auroral oval, and at ~07:10UT (panel iii) STEVE is clearly detected in LUCK. In panel iv STEVE's luminosity has increased and the whole structure has moved equatorward. In panel v several streamers can be observed at higher latitudes, while STEVE covers the whole latitudinal extent of the camera FOV. Figure 2b shows a

keogram that summarizes this event at LUCK. In this figure we can see that STEVE lasts for more than 2 hours, and appears as a narrow structure (about half a degree) equatorward of the oval. Note the luminosity gap between the auroral oval and STEVE.

To illustrate the temporal evolution differences observed for the STEVEs analyzed in this study we compared three events in Figure 3. The first two panels show data from THEMIS ASI and the last panel is from REGO. Panel a shows a keogram from 2010 April 05, in which STEVE is observed as a narrow structure measuring about ~0.4˚MLat. The structure persists for about 45 minutes and moves equatorward ~0.7˚MLat during this time. This latitudinal motion is not uniform. The structure moved about half a degree equatorward between ~05:50:00-05:55:00UT. Subsequently, STEVE moved poleward from ~05:55:00 to ~06:02:00UT, and then moved equatorward again for several minutes.

Figure 3b shows a second event on 2010 August 3 in which STEVE was observed in THEMIS ASI at The Pas (TPAS) ASI. Magnetic midnight for TPAS occurs at ~ 07:25 UT. In this event, STEVE lasted for around 15 minutes, varying in intensity. STEVE initially shows a poleward displacement of about half a degree from ~05:45:00UT to 05:54:00UT, and then moves equatorward. The total latitudinal displacement for this event is ~0.06˚ MLAT poleward. This is the only event in our dataset showing a net poleward displacement. The average displacement for all the events is presented in the following section. Figure 3c shows an event identified in LUCK REGO on 2017 September 27. During this event STEVE lasted for more than 2 hours, showing a relatively uniform equatorward displacement. Its width is about half a degree and the total latitudinal displacement is ~1.7˚MLat. A possible explanation for the average equatorward motion of STEVE is an expansion of the high-latitude convection zone, which is highlighted by the presence of auroral streamers at higher latitudes and by the equatorward auroral oval motion observed in Figure 3a and c.

3b. Statistical study of STEVE's evolution

For the 28 STEVE events identified in the THEMIS ASI and REGO databases, we calculated the latitudinal width and latitudinal displacement (equatorward or poleward) relative to STEVE's initial location. We also calculated their average duration and average longitudinal extent. Finally, we identified optical characteristics common to the events.

To determine STEVE's width, we plotted luminosity as a function of latitude every 30 seconds for each of the events (except for one case in which the analysis was made every 3s due to the short duration of the structure, which was ~15min). An example event is shown in Figure 4, in which a keogram from 07:00:00 to 08:00:00 UT is shown in the top panel. The lower panels show luminosity as a function of magnetic latitude for three different time stamps. The black line corresponds to optical data from LUCK REGO. For each of these plots we performed a Gaussian fit (pink line) around STEVE's maximum luminosity to calculate the full width at half of the maximum (FWHM). We repeated this calculation every 30 seconds (on average ~100 times per event) and then calculated the average width for that event as the average FWHM over all the curves.

To determine latitudinal displacement, we calculated the position of the maximum luminosity at the time when STEVE was first observed and compared this location with the latitude of the maximum intensity before STEVE faded away from the camera FOV. This displacement can be observed clearly in Figure 4 panel b-d. Initially (panel b), the maximum luminosity is located at around 61.1˚MLat (dashed green line). Half an hour later (panel d) STEVE's maximum luminosity is observed at ~59.7˚MLat. During these 30 minutes, STEVE moved ~0.4˚ Mlat equatorward.

Table 1 shows the statistical results obtained from the analysis explained above. From left to right the columns corresponds to average duration, width and latitudinal displacement, respectively. We see that the latitudinal width of STEVE is 20 ± 2 km and the latitudinal displacement is on average 51 ± 8 km. The uncertainties listed in the table are the standard deviation of the corresponding mean values. The difference in the average width observed by the two instruments could be associated with the fact that redline aurora is particularly sensitive to low-energy precipitation [Shepherd et al., 1980]. Even though the average width for the events identified using THEMIS ASI was approximately half of the width of the events measured by REGO, STEVE can be clearly described as an extremely narrow structure in the subauroral region. Although these are two different phenomena, it is possible to compare STEVE's width to other structures such as auroral streamers that have been characterized using the same database. Auroral streamers are the ionospheric signature of longitudinally localized earthward flow bursts in the plasma sheet and are typically observed as north-south aligned structures in the ionosphere [Henderson et al., 1998; Sergeev et al., 1999, 2000; Lyons et al., 1999, 2002; Kauristie et al., 2000; Zesta et al., 2002]. Gallardo-Lacourt [2014] determined that the average azimuthal width of auroral streamers was about 75

km in the ionosphere. STEVE only corresponds to approximately one quarter of the typical streamer width. In addition, STEVE persists longer than auroral streamers.

Table 1 shows significant differences in STEVE's width calculated using THEMIS and REGO ASI. Some of these differences are due to the sensitivity of redline ASIs to measure lower energy particles. Uncertainties in these measurements are also associated with the mapping altitudes. White light data (THEMIS) is typically mapped to 110 km altitude and redline (REGO) is mapped at 230 km. Currently, the altitude of STEVE's emissions is unknown. Spectrographic measurements are needed to obtain the true mapping altitude for the ASIs. If all optical signatures of STEVE map to the same altitude, the different mapping altitude could account for the apparent difference in width and latitudinal displacement observed by the two instruments.

Next, we calculated the average duration of STEVE between when the structure was first observed in any of the ASIs and the time it faded away or it propagated outside of the camera FOV. On average, STEVE persists for 56 ± 8 minutes, with event durations varying between 15 to 220 minutes. We also determined STEVE's longitudinal extent and found that it extends ~2145 ±198 km across the North American sector on average. Most of the STEVE events are observed across the entire longitudinal FOV of the ASIs, in that case the longitudinal extent was calculated as the ASI's longitudinal coverage. In this study there are also several events covering more than one camera FOV. It is important to note that this calculation was restricted by the longitudinal coverage of the ASIs and it is very likely that STEVE actually covers an even larger longitudinal sector. The different mapping altitudes, field of views, and sensitivity of the instruments could be responsible for the differences shown in Table 1. However, a direct comparison between REGO and THEMIS observations of the same event are needed to say this with confidence.

Figure 5a shows a histogram with STEVE's monthly distribution, spanning from January 2008 to December 2017. We can see that the events analyzed are observed between February and September with a local maximum in September. There were no events from October to January. However, the selection criteria in this study is limited by the atmospheric conditions (i.e. cloud cover). Previous studies have reported an increase in cloud cover in the US and Canada during winter months compared to summer months [Henderson-Sellers, 1989], which may be the cause for the lack of events during these months. To

clearly elucidate if this seasonal variability is real, a large scale study of the occurrence of cloud cover and other conditions preventing optimal ASI observations is required but it is beyond of the scope of the current study.

Figure 5b shows STEVE's yearly distribution. We observed higher occurrences in 2008; after which, the number of events decreased. The STEVE occurrence rate shows an increase in 2016 and 2017. At the moment, we do not have enough events to established any statistically significant trends or correlation with seasonal variations or heliospheric conditions.

4. Solar wind conditions and geomagnetic activity indices.

We have performed a superposed epoch analysis of potentially relevant space weather global indices in the hours surrounding STEVE events. The epochs were defined as the times in the optical data at which the 28 STEVE were initially observed. To determine the geomagnetic conditions under which STEVE was observed, we first analyzed Dst index from the 1-hour Kyoto database. The Dst index was introduced to study global magnetic field fluctuations during geomagnetic storm conditions and is often considered to reflect variations of the symmetric part of the ring current surrounding Earth, between 3 to 8 R_E [Dessler and Parker, 1959; Sckopke, 1996; Wanliss and Showalter, 2006]. In addition, we analyzed Kp indices for all 28 events using the OMNI 2 dataset that contains hourly solar wind magnetic field and plasma data from many spacecraft in geocentric orbit and in orbit about the L1 Lagrange point ~225 Re. Data from these satellites is then phase shifted to the magnetopause. We also used the 1-minute high-resolution OMNI database to analyze solar wind speed, dynamic pressure, magnetic field and AL index.

Figure 6a shows Dst index for the 28 events, where the red line represents the average Dst. We have assumed a normal distribution for our data and calculated confidence intervals to estimate how well our average represents the events as a whole. The blue lines in Figure 6 indicate the 99% confidence interval in all panels. In figure 6a, we have plotted the Dst index 12 hours before STEVE was first observed in the ASI data (time zero, green-dashed line) and 12 hours after. On average, the Dst index was steady around -20 nT for all events, which indicates that the observed STEVE events did not occur during particularly active geomagnetic conditions or storm times.

We also analyzed the Kp index and performed a superposed epoch analysis. These results are presented in Figure 6b, where the vertical green-dashed line indicates when STEVE was initially observed in the optical data (time zero). We plotted Kp index 5 days (120 hours) before and 2 days (48 hours) after STEVE was identified. The red line indicates the average value of Kp during this time-period. Approximately 12 hours before STEVE was observed, Kp index increased from an average below 2 to a Kp of about 3.5. Although these Kp values do not necessarily represent periods of high geomagnetic disturbance, Gussenhoven et al. [1983] showed that for Kp values between 2 and 3.5, the equatorward boundary of the diffuse aurora is located on average around 62.5˚± 3˚ Magnetic Latitude (MLat). Although it is beyond the scope of this paper, this result suggests that STEVE could be located equatorward of the diffuse aurora boundary.

In addition, we analyzed solar wind velocity and dynamic pressure using the 1-minute high resolution OMNI database. Figure 6c and d show the solar wind flow velocity and dynamic pressure 6 hours before and after STEVE was observed in the optical data (time zero). On average, the solar wind flow speed and dynamic pressure are quasi-steady at ~500-550 km/s and ~ 3nPa, respectively. In general, the average solar wind speed ranges between 400-500 km/s [Brandt, 1970], which indicates that STEVE occurs during periods of nominal solar wind speed. Similarly, the solar wind dynamic pressure was relatively steady and, with the exception of one event, no dynamic pressure shocks were observed during STEVE events.

Figure 7 shows the superposed epoch analysis for the three components of the Interplanetary Magnetic Field (IMF). From top to bottom, the panels represent the magnetic field in the x, y and z-component, respectively. The IMF spans 3 hours before and after STEVE was observed in the optical data, where time zero is highlighted by the vertical green-dashed line. The plot shows that on average B_x is positive, while B_y and B_z are mostly negative. Similar results were obtained with median IMF values. Previous studies have reported that for periods of negative B_z, the polarity of B_y influences magnetospheric convection and potentially defines the substorm's spatial extent [Friis-Christensen and Wilhjelm, 1975; Arun et al., 2005]. In addition, the location of substorm onset is statistically observed more duskward during negative B_y [Grocott et al., 2010]. Even though STEVE is not associated with high geomagnetic activity, it is interesting to note that the geomagnetic conditions observed here are similar to those observed for SAR arcs [Rees and Roble, 1975; Kozyra et al., 1997; Lobzin and Pavlov, 1999].

The last parameter we analyzed in this section is the AL index from the OMNI database. Figure 8 shows the superposed epoch analysis for the 28 STEVE events for 6 hours surrounding when STEVE was observed in the optical data (zero, vertical green-dashed line). The red line represents the average for all 28 STEVE events. From the AL perspective, STEVE occurs on average about an hour after substorm onset, at the end of the expansion phase.

We compared the typical substorm AL index with the STEVE AL indices. We analyzed the SuperMAG substorm list from 2001 to 2010 (~16k events) and performed a superposed epoch analysis three hours before and after substorm onset of AL index from the OMNI data base in figure 9a. The red line corresponds to the average AL index for the entire substorm list and the blue lines correspond to the 99% confidence interval about the mean. The light blue lines correspond to 220 events for reference (we plotted one substorm every 75 from SuperMAG substorm list). On average, the AL index decreases ~200nT during common substorms, while the STEVE events resulted in a decrease of ~300nT (from Figure 8). However, the difference in the duration of the expansion phase for SuperMAG substorms and STEVE events is perhaps one of the most interesting aspects of this comparison. On average for common substorms from the list, the expansion phase persisted for ~25min from the onset (start of the AL decrease), while for the STEVE events the duration of the expansion phase was ~60min.

STEVE has been identified in the subauroral region by McDonald et al. [2018]. In their study STEVE was co-located with a narrow and very fast flow (almost 6 km/s), which could correspond to an extreme Subauroral Ion Drift (SAID) event [Spiro et al., 1979; Archer and Knudsen, 2018]. For comparison, Figure 9b shows the superposed epoch analysis of the AL-index for the 22 SAID events identified by Archer and Knudsen [2018] using Swarm satellite. In this plot, the red line indicates the average AL index and the vertical green-dashed line corresponds to the time when the SAID fast and narrow flow signature was observed by the Swarm satellite. It is interesting to note that, on average, the minimum AL index is almost -400 nT, which is slightly smaller in magnitude than the one observed for the STEVE events in Figure 8. The Swarm observations of the SAID events appear to be located during the AL recovery phase, after a slow expansion phase, which is analogous to the AL conditions observed during STEVE events.

5. Discussion

In section 3a, we analyzed the morphology of STEVE's characteristics using ground-based all-sky cameras. We previously noted that, on average, STEVE exhibits an equatorward motion. A possible explanation for this motion is the equatorward expansion of the high-latitude convection zone. Prior to and during STEVE's appearance, we were able to identify several auroral streamers within the auroral oval that might contribute to its observed equatorward movement. This interesting connection to STEVE's motion will be addressed in future works.

We performed a statistical analysis of the optical characteristics of STEVE (section 3b) and observed significant differences in the calculation of STEVE width using both database. These discrepancies can be attributed to the difference in mapping altitudes for THEMIS and REGO. Currently, we do not have information about STEVE's emission spectrum to elucidate its precise altitude.

We also presented the monthly distributions for all 28 STEVE events identified in this paper. However, we do not have a statistically significant number of events to identified solar cycle or seasonal dependences. Moreover, to establish a trend several factors must be taken into consideration. Previous statistical studies have identified increased cloud cover over North America during the winter months [e.g., Henderson-Sellers, 1989]. In a future work, it would be interesting to calculate similar cloud cover statistics for the specific ASIs used in this analysis. The reader could also attribute the differences to seasonal light conditions, with increased insolation during the summer months (northern hemisphere). Although this is true (particularly for high-latitudes), the operation period of the mid-latitude camera's during the winter and summer months is comparable.

In section 4, we analyzed the solar wind conditions and geomagnetic indices during the 28 STEVE events. Even though STEVE is not associated with high geomagnetic activity, it is interesting to note that STEVE occurs under similar conditions as observed for SAR arcs [Rees and Roble, 1975; Kozyra et al., 1997; Lobzin and Pavlov, 1999].

Lastly, we have observed STEVE at the end of a prolonged substorm expansion phase (~60 min). The substorm expansion phase is typically characterized by injections [Lezniak and Winckler, 1970; Thomas and Hedgecock, 1975; Birn et al., 1998], which are more commonly observed for higher AL values [Gabrielse et al., 2014]. The difference in the AL indices analyzed for STEVE, SAID, and regular

substorm events suggests that STEVE develops after an extended period of injections. These injections could significantly contribute to the buildup of ring current pressure [Gkioulidou et al., 2014], which could also increase shielding in the near-Earth region [Wolf et al., 2007]. It is well known that precipitation at higher latitudes enhances ionospheric conductivities and, when combined with the effect of increased shielding, could possibly enhance mid-latitude westward flows [Southwood and Wolf, 1978]. It is possible that the strong subauroral flows observed during the STEVE event reported by MacDonald et al [2018] could be related to the extended expansion phase observed in our results. Gallardo-Lacourt et al. [2017] analyzed enhancements in the westward flow speed in the subauroral region associated with the intensity of the auroral streamers; they reported a weak correlation between these parameters. However, the AL observations presented in this paper could unveil the link between the high and mid-latitude regions of the ionosphere during STEVE events. Overall, more analysis beyond the scope of this paper is required; an explanation for the luminosity of STEVE is also needed.

6. Conclusions

By taking advantage of the high temporal and spatial coverage provided by THEMIS ASI and REGO database we conducted a statistical analysis of the properties of 28 STEVE events.

We identified events in THEMIS ASI from December 2007 to December 2015 (21 events) and in REGO (7 events) from November 2015 to December 2017. We determined that, on average, STEVE's duration was about one hour and its latitudinal width was ~20km. STEVE's typical latitudinal displacement was also, on average, about 50 km during its entire duration. This displacement is equatorward for most of the events; only one of the 28 events showed net poleward displacement. We also measured STEVE's longitudinal extent and found that the structure extends ~2145 km across the North American sector.

We found that the typical Dst index for these events was relatively moderate at ~20 nT and that Kp index increases from 2 to 3.5 about 12 hours before STEVE was observed. In addition, the average solar wind speed and dynamic pressure for our events was ~550 km/s and ~3 nPa, respectively. Only one of these events corresponded to a shock associated with a pressure increase about one hour before STEVE was observed.

IMF conditions during the STEVE events showed that, on average, IMF B_x was positive approximately 3 hours before and after STEVE. Interestingly, IMF B_y and B_z were negative (on average) during our events, suggesting a connection between STEVE and the polarity of the IMF components. This aspect will be analyzed and addressed in the future.

In the superposed epoch analysis of the AL index, we found that STEVE occurs about 1 hour after substorm onset at the end of the expansion phase. We compared this result with AL indices observed for SAIDs and regular substorms from the SuperMAG database and found that the magnitude of AL was higher and that the expansion phase had a longer duration (~1 hour) during STEVE events. These results suggest that in order for STEVE to be observed, a large number of the injections must occur in the plasma sheet. Perhaps these injections effectively increase the ring current pressure and further enhance the subauroral westward flows, an effect that is consistent with the Swarm observations from McDonald et al. [2018].

Acknowledgments

Bea Gallardo-Lacourt would like to thank Dr. Hsien-Liang Tseng from the Air Force Institute of Technology (AFIT) for insightful discussions. The authors also thank the Alberta Aurora Chasers for actively reporting events in their website. This work was supported by NASA grant NNX17AL22G, NSF grants PLR-1341359 and AGS-1737823, and AFOSR FA9550-15-1-0179 and FA9559-16-1-0364. The THEMIS mission is supported by NASA contract NAS5-02099, NSF grant AGS-1004736, and CSA contract 9F007-046101. REGO is supported by the Canadian Space Agency (CSA-1006482).The THEMIS and REGO ASI data can be obtained from http://data.phys.ucalgary.ca/. OMNI data and SuperMAG data were obtain through https://omniweb.gsfc.nasa.gov/ and http://supermag.jhuapl.edu respectively. We acknowledge the support of the Natural Science and Engineering Research Council of Canada (NSERC) Discovery Grant Program and Discovery Accelerator Supplement Program grant RGPIN/06069-2014.

REFERENCES

Archer, W. E., & Knudsen, D. J. (2018). Distinguishing subauroral ion drifts from Birkeland current boundary flows. Journal of Geophysical Research: Space Physics, 123. doi: 10.1002/2017JA024577.

Arun T., A. Dhar, K. Emperumal, B.M. Pathan (2005). IMF B_Y dependence of the extent of substorm westward electrojet. J. Earth Syst. Sci., 114 (2005), pp. 177-184.

Birn, J., M. F. Thomsen, J. E. Borovsky, G. D. Reeves, D. J. McComas, R. D. Belian, and M. Hesse (1998), Substorm electron injections: Geosynchronous observations and test particle simulations, J. Geophys. Res., 103(A5), 9235–9248, doi:10.1029/97JA02635.

Brandt, J. C. (1970), Introduction to the Solar Wind, San Francisco, W. H. Freeman and Company.

Dessler, A. J., and E. N. Parker (1959), Hydromagnetic theory of geomagnetic storms, J. Geophys. Res., 64(12), 2239–2252, doi:10.1029/JZ064i012p02239.

Friis-Christensen E and Wilhjelm (1975), Polar cap currents for different directions of the interplanetary magnetic field in the y-z plane; J. Geophys. Res. 80 1248–1260.

Gabrielse, C., V. Angelopoulos, A. Runov, and D. L. Turner (2014), Statistical characteristics of particle injections throughout the equatorial magnetotail, J. Geophys. Res. Space Physics, 119, 2512–2535, doi:10.1002/2013JA019638.

Gallardo-Lacourt, B., Y. Nishimura, L. R. Lyons, S. Zou, V. Angelopoulos, E. Donovan, K. A. McWilliams, J. M. Ruohoniemi, and N. Nishitani (2014), Coordinated SuperDARN THEMIS ASI observations of mesoscale flow bursts associated with auroral streamers, J. Geophys. Res. Space Physics, 119, 142–150, doi:10.1002/2013JA019245.

Gallardo-Lacourt, B., Nishimura, Y., Lyons, L. R., Mishin, E. V., Ruohoniemi, J. M., Donovan, E. F., Angelopoulos, V., & Nishitani, N. (2017). Influence of auroral streamers on rapid evolution of ionospheric SAPS flows. Journal of Geophysical Research: Space Physics, 122, 12,406–12,420. https://doi.org/10.1002/2017JA024198.

Gallardo-Lacourt, B., Liang, J., Nishimura, Y., & Donovan, E. (2018). On the origin of STEVE: Particle precipitation or ionospheric skyglow? GRL, 45. https://doi.org/10.1029/2018GL078509

Gjerloev, J. W. (2009), A Global Ground-Based Magnetometer Initiative, Eos Trans. AGU, 90(27), 230–231, doi:10.1029/2009EO270002.

Gjerloev, J. W. (2012), The SuperMAG data processing technique, J. Geophys. Res., 117, A09213, doi: 10.1029/2012JA017683.

Gkioulidou, M., A. Y. Ukhorskiy, D. G. Mitchell, T. Sotirelis, B. H. Mauk, and L. J. Lanzerotti (2014), The role of small-scale ion injections in the buildup of Earth's ring current pressure: Van Allen Probes observations of the 17 March 2013 storm, J. Geophys. Res. Space Physics, 119, 7327–7342, doi: 10.1002/2014JA020096.

Grocott, A., S. E. Milan, T. K. Yeoman, N. Sato, A. S. Yukimatu, and J. A. Wild (2010), Superposed epoch analysis of the ionospheric convection evolution during substorms: IMF B_Y dependence, J. Geophys. Res., 115, A00I06, doi:10.1029/2010JA015728.

Gussenhoven, M. S., D. A. Hardy, and N. Heinemann (1983), Systematics of the equatorward diffuse auroral boundary, J. Geophys. Res., 88(A7), 5692–5708, doi:10.1029/JA088iA07p05692.

Henderson, M. G., G. D. Reeves, and J. S. Murphree (1998), Are north-south structures an ionospheric manifestation of bursty bulk flows?, Geophys. Res. Lett., 25, 3737–3740.

Henderson-Sellers, A (1989), North American total cloud cover amount variations this century, Global Planetary Change, 75: 175-194.

Kauristie,K.,V.A. Sergeev,M.Kubyshkina, T. I. Pulkkinen, V. Angelopoulos, T. Phan, R. P. Lin, and J. A. Slavin (2000), Ionospheric current signatures of transient plasma sheet flows, J. Geophys. Res., 105, 10,677–10, 688.

Kozyra, J. U., A. F. Nagy, and D. W. Slater (1997), High -altitude energy arcs, Rev. Geophys., 35(2), 155–190, doi:10.1029/96RG03194.

Lezniak, T. W., and J. R. Winckler (1970), Experimental study of magnetospheric motions and the acceleration of energetic electrons during substorms, J. Geophys. Res., 75(34), 7075–7098, doi:10.1029/JA075i034p07075.

Liang, J., E. Donovan, B. Jackel, E. Spanswick, and M. Gillies (2016), On the 630 nm pulsating aurora: Red-line Emission Geospace Observatory observations and model simulations, J. Geophys. Res. Space Physics, 121, 7988–8012, doi:10.1002/2016JA022901.

V. V. Lobzin, A. V. Pavlov, Correlations between SAR arc intensity and solar and geomagnetic activity, Annales Geophysicae, European Geosciences Union, 1999, 17 (6), pp.770-781.

Lyons, L. R., T. Nagai, G. T. Blanchard, J. C. Samson, T. Yamamoto, T. Mukai, A. Nishida, and S. Kokobun (1999), Association between Geotail plasma flows and auroral poleward boundary intensifications observed by CANOPUS photometers, J. Geophys. Res., 104, 4485–4497.

Lyons, L. R., E. Zesta, Y. Xu, E. R. Sanchez, J. C. Samson, G. D. Reeves, J. M. Ruohomiemi, and J. B. Sigwarth (2002), Auroral poleward boundary intensifications and tail bursty flows: A manifestation of a large-scale ULF oscillation?, J.Geophys. Res., 107(A11), 1352, doi:10.1029/2001JA000242.

MacDonald, E. A., E. F. Donovan, Y. Nishimura, N. A. Case, D. M. Gillies, B. Gallardo-Lacourt, W. E. Archer, E. L. Spanswick, N. Bourassa, M Connors, M. Heavner, B. Jackel, B. Kosar, D. J. Knudsen, C. Ratzlaff, and I. Schofield (2018), New Science in Plain Sight: Citizen Scientists Lead to Discovery of Optical Structure in the Upper Atmosphere, *Accepted in Science*.

Mende, S. B., S. E. Harris, H. U. Frey, V. Angelopoulos, C. T. Russell, E. Donovan, B. Jackel, M. Greffen, and M. Peticolas (2008), The THEMIS array of ground-based observatories for the study of auroral substorms, Space Sci. Rev., 141, 357, doi:10.1007/s11212-008-9380-x.

Newell, P. T., and J. W. Gjerloev (2011), Evaluation of SuperMAG auroral electrojet indices as indicators of substorms and auroral power, J. Geophys. Res., 116, A12211, doi:10.1029/2011JA016779.

Olsen, N., Friis-Christensen, E., Floberghagen, R. et al. Earth Planet Sp (2013) 65: 1. https://doi.org/10.5047/eps.2013.07.001

Rees, M. H., and R. G. Roble (1975), Observations and theory of the formation of stable auroral red arcs, Rev. Geophys., 13(1), 201–242, doi:10.1029/RG013i001p00201.

Sergeev, V. A., K. Liou, C.-I. Meng, P. T. Newell, M. Brittnacher, G. Parks, and G. D. Reeves (1999), Development of auroral streamers in association with localized impulsive injections to the inner magnetotail, Geophys. Res. Lett., 26(3), 417–420.

Sergeev, V. A., et al. (2000), Multiple spacecraft observation of a narrow transient plasma jet in the Earth's plasma sheet, Geophys. Res. Lett., 27(6), 851–854.

Sckopke, N. (1966), A general relation between the energy of trapped particles and the disturbance field near the Earth, J. Geophys. Res., 71(13), 3125–3130, doi:10.1029/JZ071i013p03125.

Shepherd, G., J. Winningham, F. Bunn, and F. Thirkettle (1980), An empirical determination of the production efficiency for auroral 6300-Å emission by energetic electrons, J. Geophys. Res., 85(A2), 715–721, doi:10.1029/JA085iA02p00715.

Southwood, D. J., and R. A. Wolf (1978), An assessment of the role of precipitation in magnetospheric convection, J. Geophys. Res., 83(A11), 5227–5232, doi:10.1029/JA083iA11p05227.

Spiro, R. W., Heelis, R. A., & Hanson, W. B. (1979). Rapid subauroral ion drifts observed by atmosphere explorer C. Geophysical Research Letters, 6(8), 657–660

Thomas B.T., and P. C. Hedgecock (1975), Substorm Effects on the Neutral Sheet Inside 10 Earth Radii, in The Magnetospheres of the Earth and Jupiter, Edited by P. Formisano, p. 55, D. Reidel, Norwell, Mass., 1975.

Wanliss, J. A., and K. M. Showalter (2006), High-resolution global storm index: *Dst* versus SYM-H, J. Geophys. Res., 111, A02202, doi:10.1029/2005JA011034.

Wolf, R. A., R. W. Spiro, S. Sazykin, and F. R. Toffoleto (2007), How the Earth's inner magnetosphere works: An evolving picture, J. Atmos. Sol.-Terr. Phys., 69, 288

Zesta, E., E. Donovan, L. Lyons, G. Enno, J. S. Murphree, and L. Cogger (2002), The two-dimensional structure of auroral poleward boundary intensification (PBIs), J. Geophys. Res., 107(A11), 1350, doi:10.1029/ 2001JA000260

Zou, Y., Y. Nishimura, L. R. Lyons, K. Shiokawa, E. F. Donovan, J. M. Ruohoniemi, K. A. McWilliams, and N. Nishitani (2015), Localized polar cap flow enhancement tracing using airglow patches: Statistical properties, IMF dependence, and contribution to polar cap convection. J. Geophys. Res. Space Physics, 120, 4064–4078. doi: 10.1002/2014JA020946.

Figure 1. Example of a STEVE event observed using THEMIS ASI on April 05, 2010. (a) Temporal evolution of STEVE observed at ATHA ASI. The white dashed contour corresponds to 60˚ magnetic latitude. (b) Keogram summarizing the event.

Figure 2. Example of a STEVE event observed using REGO on 2017 September 27. (a) Temporal evolution of STEVE observed at Lucky Lake (LUCK). Gillam (GILL) all-sky imager provides data at higher latitudes (b) LUCK keogram summarizing the event.

Figure 3. Keograms for three STEVE events to compare differences in their temporal evolution. (a) Keogram from THEMIS ASI at Athabasca (ATHA) on 2010 April 05. (b) Keogram from THEMIS ASI at The Pas (TPAS) on 2010 August 03. (c) Keogram from REGO LUCK on 2017 September 27.

Figure 4. Methodology used to calculate STEVE's width and latitudinal propagation. (a) LUCK keogram for STEVE on 2017 September 27. This keogram is made from longitudinal cuts along the ASI central meridian. (b-d) Luminosity as a function of latitude for three different time stamps from the keogram (cyan line in (a)). The magenta line indicates the Gaussian fit. Green dashed line shows the location of STEVE's maximum luminosity.

Figure 5. (a) Histogram of STEVE occurrence binned by (a) month and (b) year.

Figure 6. Superposed epoch analysis of 28 STEVE events from THEMIS ASI and REGO database for (a) Dst index, (b) Kp index, (c) Solar wind speed, and (d) solar wind dynamic

pressure. Red lines indicate the average and blue lines indicate the 99% confidence interval. The vertical green dashed line corresponds to the time when STEVE is initially observed in the ASI data.

Figure 7. IMF Superposed epoch analysis for 28 STEVE events for (a) IMF B_x, (b) B_y, and (c) B_z, retrieved from the OMNI database. Red lines indicate the average and blue lines indicate the 99% confidence interval. The vertical green dashed line corresponds to the time when STEVE is initially observed in the ASI data.

Figure 8. AL index superposed epoch analysis for 28 STEVE events. Red lines indicate the average and blue lines indicate the 99% confidence interval. The vertical green dashed line corresponds to the time when STEVE is initially observed in the ASI data.

Figure 9. AL index superposed epoch analysis (a) 22 SAID events identified by Archer and Knudsen [2018], and (b) SuperMAG substorm onset list, in the same format as Figure 8.

Table 1. From left to right the columns represents STEVE's average duration, average width and average latitudinal displacement respectively. This data is analyzed for THEMIS ASI (first row), REGO database (second row) and an average of both databases (third row).

	Average duration (min)	average width (km)	Latitudinal displacement (km)
THEMIS ASI	50±7	15 ± 2	43 ± 8
REGO	74±24	32 ± 5	74 ± 20
TOTAL	56 ± 8	20 ± 2	51 ± 8

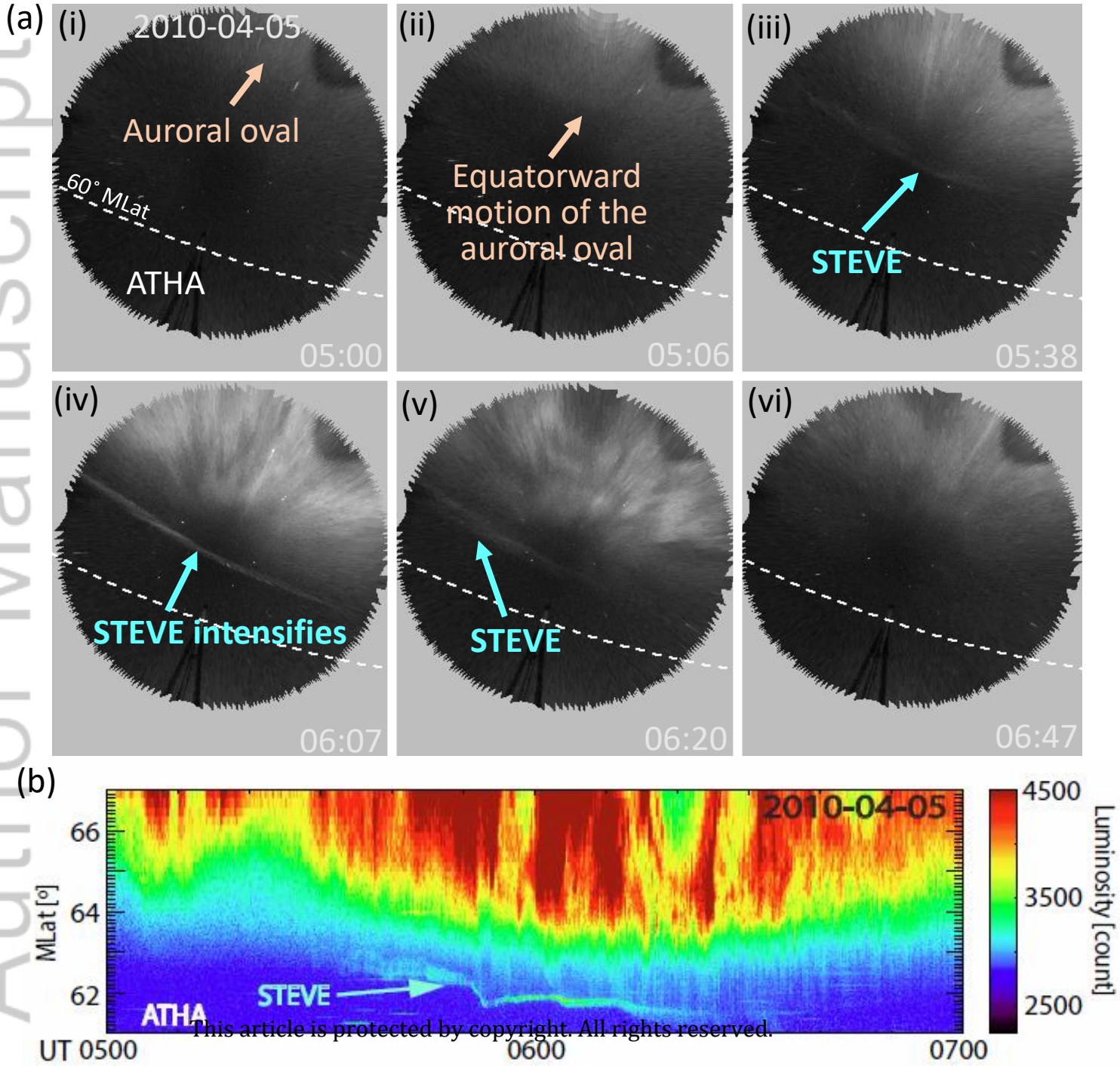

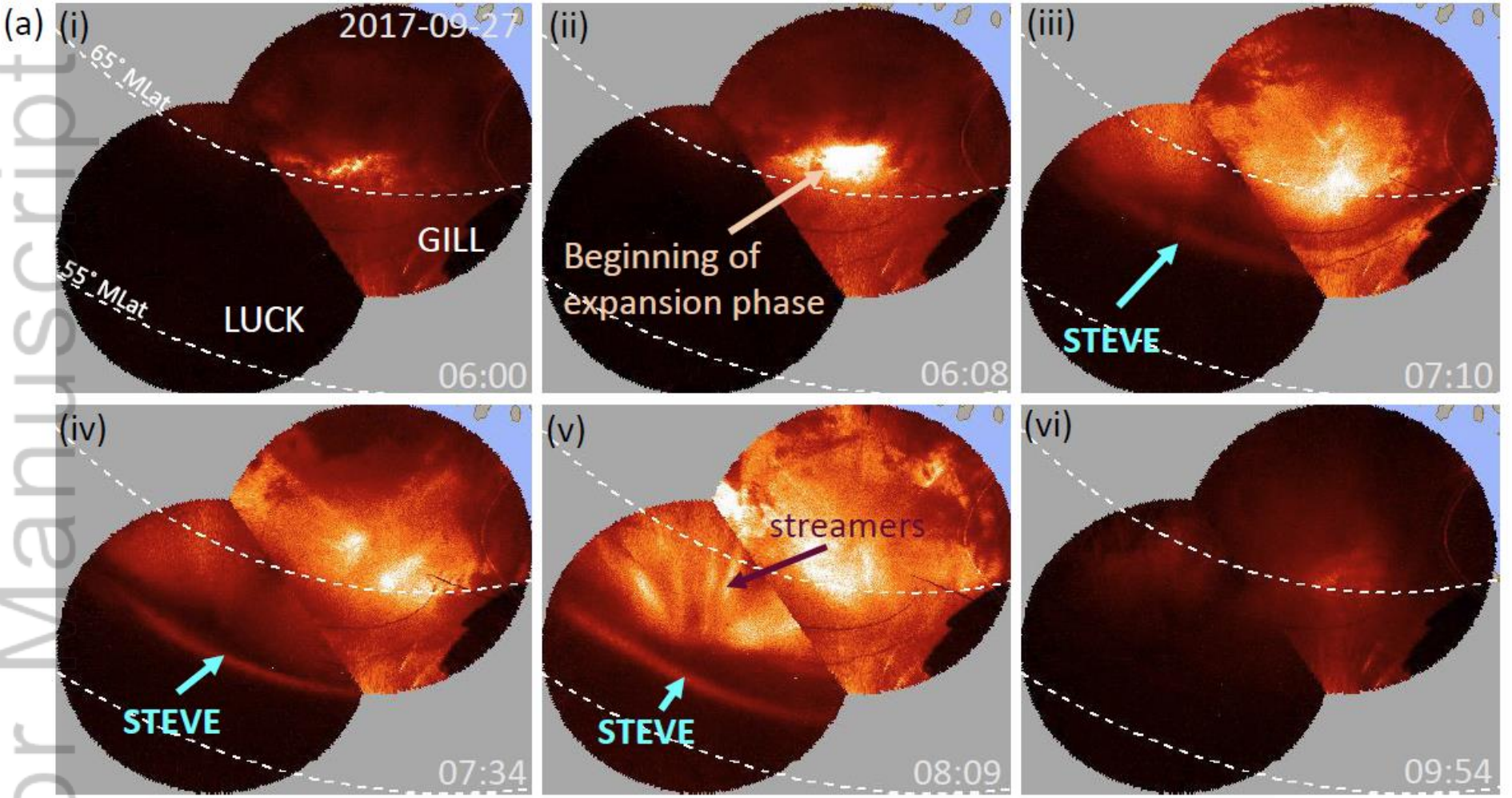

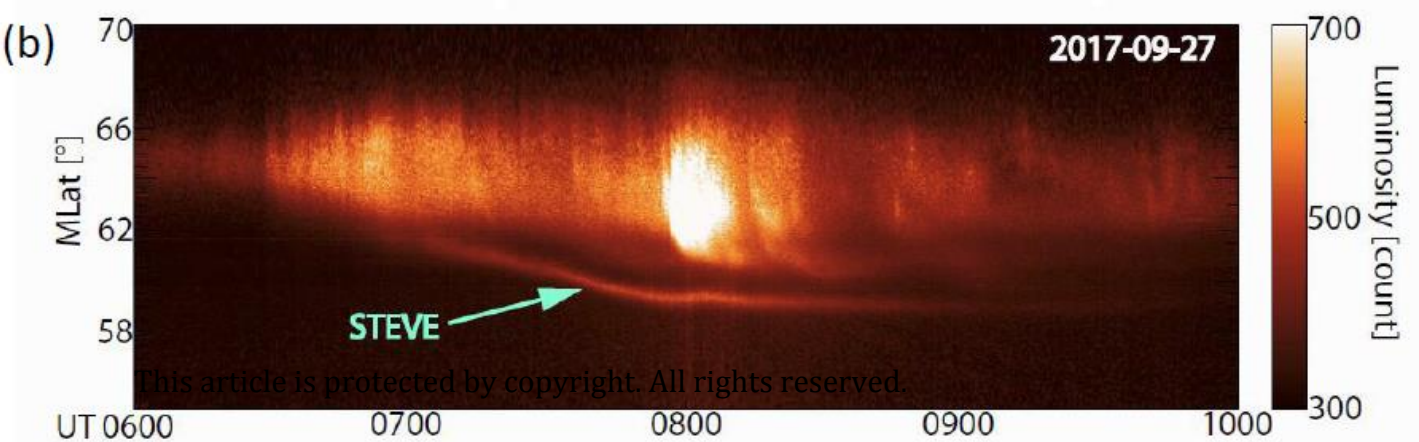

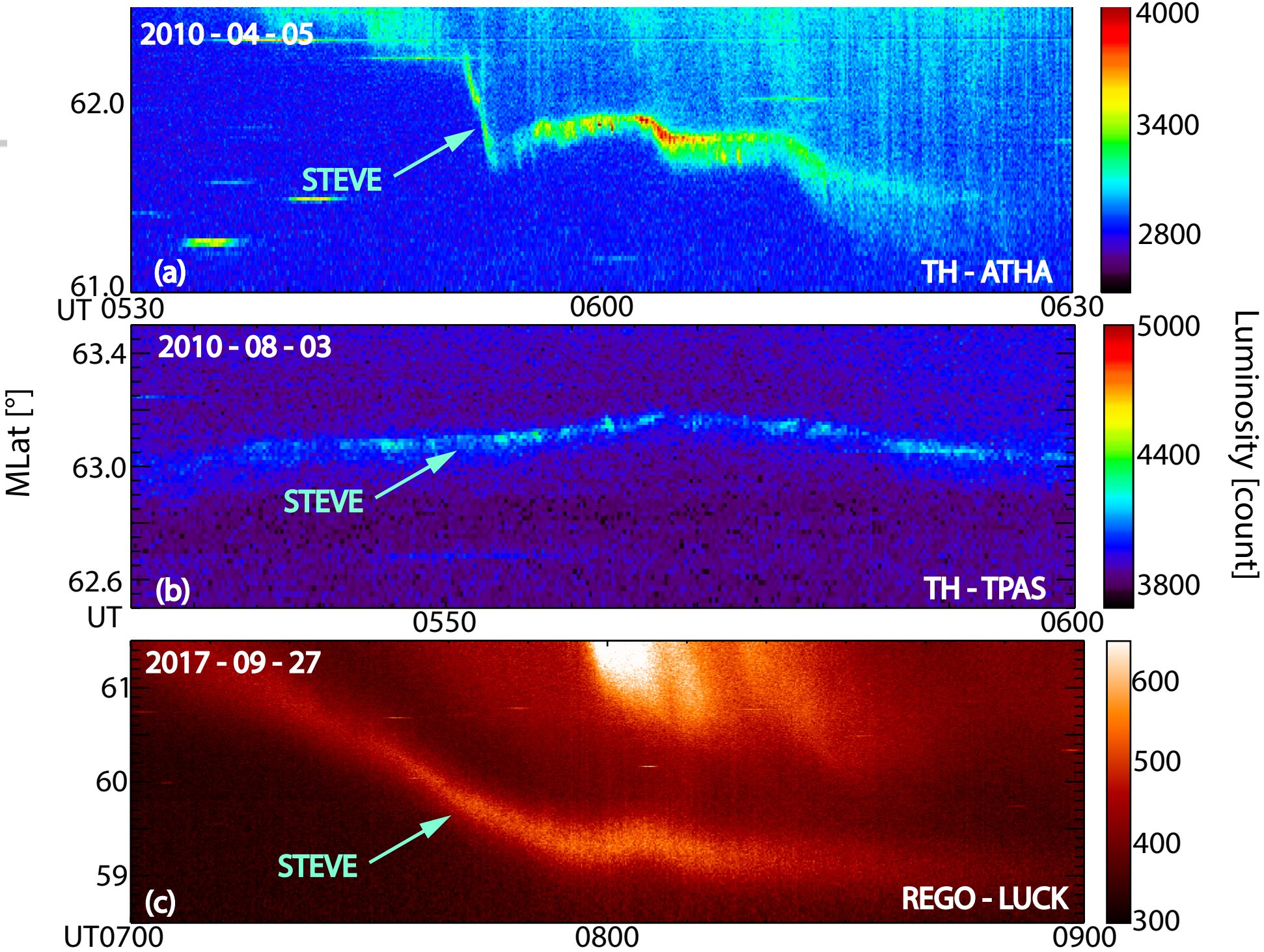

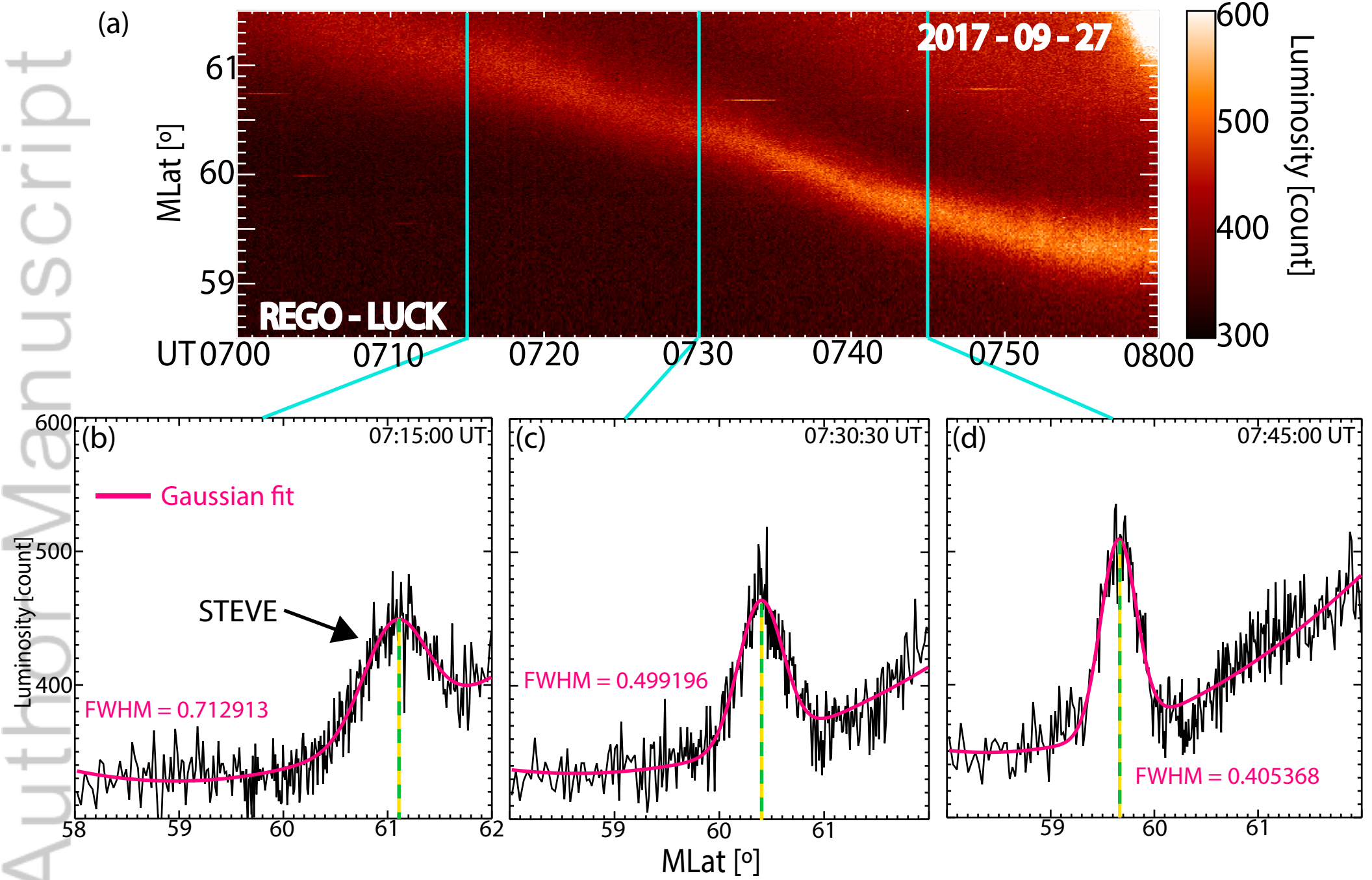

(a)

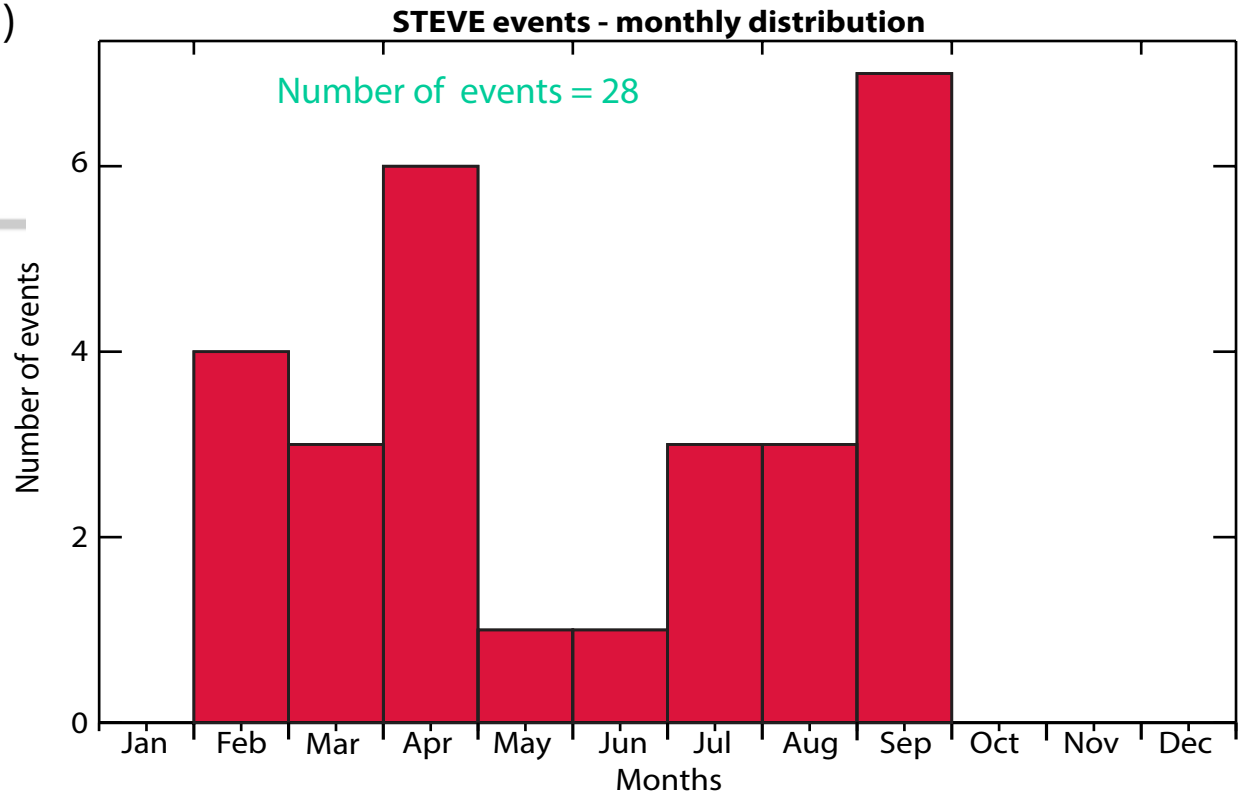

(b)